Pore Morphology of Porous Polymer Particles Probed by NMR Relaxometry and NMR Cryoporometry

Eddy W. Hansen,*,† Geir Fonnum,‡ and Ellen Weng‡

Department of Chemistry, University of Oslo, P.O. Box 1033, Blindern, NO-0315 Oslo, Norway, and Invitrogen Corporation, P.O. Box 228, 2001 Lillestrøm, Norway

Received: September 13, 2005; In Final Form: October 5, 2005

The pore size distribution (PSD) and pore connectivity (PC) within porous polymer particles are probed by combining NMR cryoporometry and NMR relaxometry (spin−spin relaxation). With water as a probe molecule, the constant K in the so-called Gibbs−Thompson equation and the surface relaxivity (ρ_2) were determined to be $K = (420 \pm 50)$ KÅ and $\rho_2 = (0.44 \pm 0.01) \times 10^{-6}$ ms^{-1}, respectively. Also, the thickness of the interface layer was estimated to be of the order of one monolayer of water molecules. A detailed analysis of the complete set of NMR data enabled the morphology or pore structure to be probed, and is thoroughly discussed in the text.

Introduction

The morphology of porous media plays an important role in the physical and chemical properties of porous materials, in particular the dynamic properties of pore-confined molecules[1−11] Also, insight into the three-dimensional porous network is of technological significance for heterogeneous catalysis, membrane separation, lubrication, and oil recovery. Porous media can be explored by a variety of experimental techniques, including mercury intrusion, N$_2$-adsorption, neutron scattering, DSC (Differential Scattering Calorimetry), imbibition, thermoporometry, NMR cryoporometry, and NMR relaxometry. Due to the general complexity of a three-dimensional porous network, it is of advantage to combine several experimental techniques to characterize porous media. Such complimentary techniques can provide more information on the pore structure and surface properties than a single technique alone.[12−18]

In the present work, the main objective is to probe the pore morphology or pore structure within porous polymer particles by combining NMR cryoporometry[19−23] and NMR relaxometry[24,25] together with N$_2$-adsorption.[25] The latter technique is used as a reference technique to determine the surface-to-volume (S/V) ratio of the smaller pores within the polymer particles. A detailed outline of this combined experimental approach is presented.

Experimental Section

Sample Preparation. The spherical porous polymer particles (polystyrene particles cross-linked with divinylbenzene) of size 2.5 μm, on average (Figure 1), were prepared by Invitrogen Corporation and presaturated with water before being gently packed into 10 mm outer diameter NMR tubes and sealed.

The sample height was restricted to approximately 10 mm to ensure the sample, located within the transmitter/receiver coil, to be homogeneously irradiated. Moreover, this constraint in sample size minimizes any temperature gradient building up
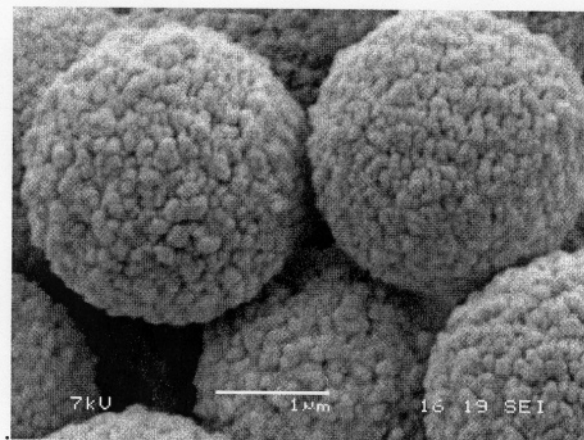
* To whom correspondence should be addressed. Phone: +4722855692. Fax: +4722855441. E-mail: eddywh@kjemi.uio.
† University of Oslo.
‡ Invitrogen Corporation.

Figure 1. SEM image of the polymer particles (Sample S107).

along the sample direction. One complicating factor concerning some porous polymer materials relates to changes in the porous network upon addition of fluids. During drying, the pores may shrink or, in the extreme case, collapse.

The reason for using water as a probe molecule in the NMR measurement is that (1) the diameter of the polymer particles remains approximately the same as for dry particles, (2) some of the larger pores that collapse during drying seem to reappear after water treatment, (3) the inner surface of the polymer particles becomes hydrophilic upon addition of water because of the nitro groups on the polymer surface (this latter property is of particular advantage when applying the NMR relaxometry technique to probe the PSD, and will be detailed later), and (4) the water molecules are small enough to enter the minor pores within the polymer sample.

NMR Measurement. All NMR measurements are performed on a low-field MARAN Ultra NMR instrument operating at 23.5 MHz proton resonance frequency, using sample tubes of 10 mm outer diameter. The spin−spin relaxation time T_2 was determined by using a CPMG pulse sequence. If not otherwise stated, a shortest possible interpulse distance 2τ (=60 μs) between successive π-pulses was applied. Since the transverse

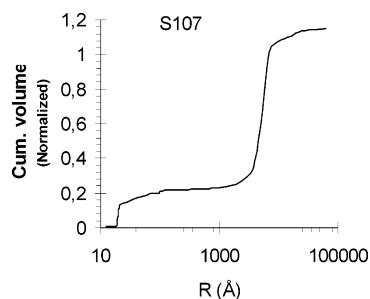**24296** *J. Phys. Chem. B, Vol. 109, No. 51, 2005*

Hansen et al.

Figure 2. Cumulative pore volume as a function of pore size (sample S107) obtained from N$_2$-adsorption.

TABLE 1: Pore Volume (*V*) and Surface Area (*S*) of Selected Pore Size Windows (Δ*R*) in Sample S107, As Obtained from Nitrogen Adsorption Data (Figure 2)

Δ*R* (Å)	*V* (cm^3/g)	*V* (%)	*S* (m^2/g)	$S/V \times 10^{-8}$ (m^{-1})	$R_{av}{}^a$ (Å)
500−5000	0.372	62.6	3.8	0.10	1958
200−500	0.005	0.8	0.3	0.60	333
50−200	0.041	6.9	11.6	2.83	71
0−50	0.177	29.7	140	7.91	25.3

^{a} Determined by assuming cylinder pore geometry, i.e., $S/V = 2/R$.

relaxation time of solid ice is very short ($T_2 = 6$ μs), whereas the corresponding relaxation time of water in a porous material is larger by some orders of magnitude, only the mobile pore water will be detected. The $\pi/2$ rf-pulse and the dwell time were set to 2.15 μs and 0.1 μs, respectively. The time delay between the end of the rf-pulse and the initiation of signal sampling (dead time) was set to 5 μs to circumvent noise from the rf-pulse to enter the receiver.

A reasonable signal-to-noise (S/N) ratio was obtained after 64 transients with a time delay of 10 s between successive transients. The latter ensures quantitative sampling of the NMR signal at any applied temperature. The temperature was calibrated by inserting two thermocouples into an NMR tube, containing methanol at a height of 10 mm. One thermocouple was placed at the top and the other at the bottom of the methanol sample. A careful calibration revealed a temperature gradient along the sample direction of approximately 1 K at a temperature of 273 K. The temperature gradient increased slightly with decreasing temperature. The temperature stability was better than 0.5 K over 24 h. During the variable-temperature experiment (NMR cryoporometry) the temperature was changed at a rate of approximately 8 deg K/h, which ensured an adequate time for temperature equilibration.

N$_2$-Adsorption/Desorption. The adsorption/desorption isotherms of nitrogen were acquired with a Carlo Erba Milestone 100 instrument. A thermistor probe controlled the temperature of the liquid-nitrogen bath. Each sample was degassed at 433 K for 1 h until a pressure of approximately 7 Torr was attained. The desorption step was initiated after a saturation pressure of 760 Torr was reached.

Results and Discussion

Nitrogen Desorption. The cumulative pore volume as a function of pore radius, as obtained from the nitrogen adsorption isotherm, is plotted in Figure 2 and the numerical data are tabulated in Table 1.

Also, the surface area and pore volume of the smaller pores (0 < *R* < 50 Å) within five additional and analogous polymer samples were measured and the results are summarized in Table 2.

NMR Cryoporometry. The theoretical basis of this NMR technique relies on the well-known Gibbs−Thompson equa-

TABLE 2: Pore Volume (*V*) and Surface Area (*S*) of the Smaller Pores (0 < *R* < 50 Å) in Five Additional Polymer Samples, As Determined from Nitrogen Adsorption Measurements

sample	*V* (cm^3/g)	*S* (m^2/g)	$S/V \times 10^{-8}$ (m^{-1})	R^a (Å)
S101	0.193	135	6.99	28.6
S125	0.179	133	7.43	26.9
S131	0.199	142	7.14	28.0
S133	0.209	184	8.80	22.7
S141	0.154	108	7.01	28.5

^{a} Determined by assuming cylinder pore geometry, i.e., $S/V = 2/R$.

tion,[19−23,27] which relates the freezing point depression (Δ*T*) of a pore confined fluid to the pore radius (*R*), according to

$$\Delta T = T_0 - T = \frac{2\gamma T_0}{R\rho\Delta H} \tag{1}$$

where T_0 is the normal bulk melting point, *T* is the melting point of the confined solid, γ is the crystal−liquid interfacial energy, ΔH is the bulk enthalpy of fusion, and ρ is the density of the frozen liquid (solid). It is assumed that γ is isotropic and that the crystal size is large enough so the confined liquid retains its bulk properties ΔH and ρ. Finally, it is assumed that the contact angle of melting crystals is 180°. There is some controversy about the validity of these assumptions, which is discussed extensively in the literature.[19,20] In short, assuming all the parameters in eq 1 to be independent of temperature and pore dimension, this equation takes the rather simple form[19,20]

$$\Delta T = K\frac{1}{R} \tag{2}$$

where *K* is a constant depending solely on the physical properties of the pore confined solid (ice). Measurement of the proton NMR signal intensity (*I*) of the pore confined water vs temperature (*T*), denoted an IT curve (eq 3),[22] was determined from the observed CPMG echo curve by estimating the intensity at zero time.

$$I(X) = \sum_{i=1}^{N} \frac{I_{01}}{\sqrt{\pi}} \int_{-\infty}^{(X-X_{ci})/\sqrt{2\Delta_i}} \exp[-u^2]\,\mathrm{d}u \tag{3}$$

The latter was determined by model fitting a sum of four exponential functions to the observed CPMG-echo curve (with $2\tau = 60$ μs, see previous section; NMR measurements). This signal intensity was corrected for temperature by implementing the Curie law, i.e., the observed signal intensity was multiplied by the factor T/T_0 with $T_0 = 273.15$ K and *T* defining the actual temperature. Also, the PSD (d*I*/d*R*) can be determined from the derivative of the IT curve with respect to the absolute temperature, i.e.,

$$\frac{\mathrm{d}I}{\mathrm{d}R} = -\frac{K}{R^2}\cdot\frac{\mathrm{d}I}{\mathrm{d}T} \tag{4}$$

where X_{ci} (=$1000/T_{ci}$). T_{ci} and Δ_i represent the melting point transition and the width of the corresponding melting curve. The sharper the transition, the smaller is Δ_i.

The model fitted IT curve (eq 3) of water confined in the porous polymer sample (S107) is plotted in Figure 3 (solid curve). The number (*N*) of temperature transitions was determined by a statistical significance test. As can be inferred from Figure 3, the residuals are randomly distributed.
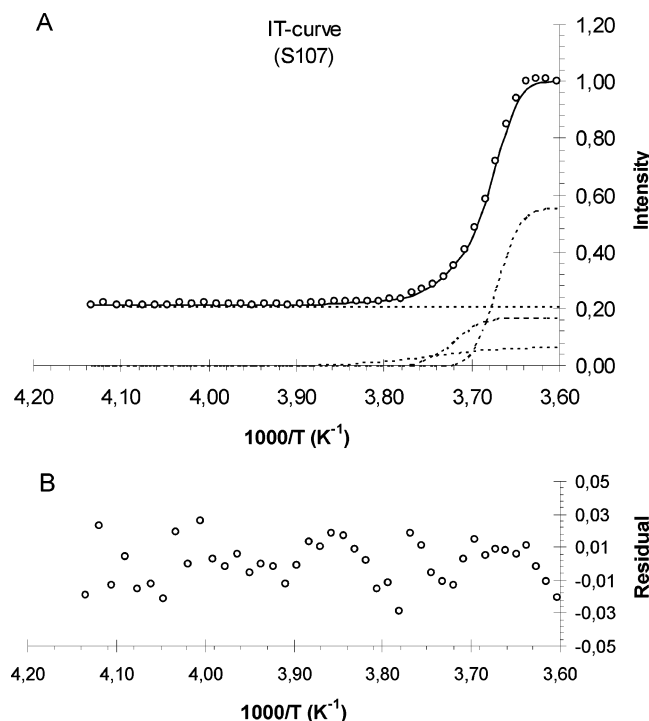
Pore Morphology of Porous Polymer Particles

J. Phys. Chem. B, Vol. 109, No. 51, 2005 **24297**

Figure 3. (A) The intensity of water confined within the polymer sample (S107) as a function of temperature (IT curve) is shown as open circles. The model-fitted IT curve (eq 4) is represented by the solid curve. Each one of the four individual IT curves is represented by dotted curves. (B) The residual between observed and model-fitted (eq 4) IT curves.

Figure 4. Melting point distribution curve (dI/dX) of water confined in sample 107 showing three distinct and different regions B, C, and D. The solid curve represents the cumulative signal intensity (IT curve) as a function of temperature (see also Figure 3). Region A, which represents the lower temperature transition, was unable to be determined due to experimental limitations. See text for further details.

TABLE 3: Intensity (I_{0i}), Inverse Temperature Transition X_{ci} ($=1000/T_{ci}$), Width of the Temperature Transition (Δ_i), and the Melting Point Depression (ΔT) of Each Transition (i), As Obtained by Model-Fitting (Eq 4) to the Observed IT Curve of Sample S107 (Figure 3)

transition i (region)	$X_{ci}{}^a$	$\Delta_i{}^b$	$I_{0i}{}^c$ (%)	ΔT (K)	R^d (Å)
1 (D)	3.671	0.015	55	0.75	560
2 (C)	3.721	0.019	17	5.13	82
3 (B)	3.754	0.049	7	6.77	62
4 (A)			21		

a Uncertainty is estimated to be less than ±0.003. *b* Uncertainty is estimated to be approximately ±5%. *c* Uncertainty is estimated to be approximately ±10%. *d* Determined from eq 2 with $K = 420$ KÅ. K was determined from NMR relaxometry, and will be discussed in a later section.

The numerical values of the model fitted parameters are tabulated in Table 3. Unfortunately, since the instrument is unable to generate any temperature below approximately 238 K, the lower transition temperature ($i = 4$) could not be determined by the NMR cryoporometry approach, only its intensity, and will be commented on in a later section.

The melting point distribution dI/dX of the pore confined solid water (ice) may be derived by differentiation of the IT curve (Figure 3A) with respect to temperature ($X = 1000/T$), and is plotted in Figure 4.

The numerical values derived by model fitting to eq 4 are summarized in Table 3. Although NMR cryoporometry is a simple and straightforward experimental technique for probing PSD, it has some restrictions, related to how well the temperature can be controlled, i.e., to what degree the absolute temperature can be determined and to what extent any temperature gradient exists across the sample. In normal cases, the temperature can be determined accurately only to within ±0.5
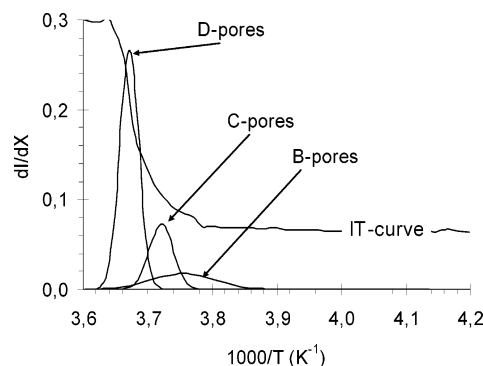
K, implying that any pores larger than $2K$ (where K is the parameter defined in eq 2) cannot be resolved. Hence, the technique is optimally suited for smaller pores, i.e., pores smaller than K (approximately 420 Å in this work). The pore resolution improves for fluids having larger K. Also, as can be inferred from eq 2, the pore resolution improves with decreasing temperature.

However, by improving the instrumental design, the temperature control can be significantly improved (±0.1 K should be within reach).

Note, when applying the CPMG pulse sequence on a dry polymer sample ($2\tau = 60$ μs) no signal was detected.

NMR Relaxometry. Due to Brownian motion, water molecules will move randomly within a pore structure and hence affect the transverse relaxation time T_2. Without going into details it is well documented, over decades, that the relaxation rate $1/T_2$ of a fluid confined in a single pore can be expressed by[13,15,24,28-31]

$$\frac{1}{T_2} = \frac{1}{T_{2,B}} + \frac{S}{V} \cdot \rho_2 \quad (5A)$$

$$\rho_2 = \frac{\lambda}{T_{2,S}} \quad (5B)$$

where λ represents the thickness of the interface water, which is located between the polymer matrix and the solid ice within the pore. $T_{2,B}$ and $T_{2,S}$ represent the spin–spin relaxation times of bulk water and surface water, respectively, and ρ_2 defines the surface relaxivity (which should not be confused with the fluid density, which is assigned the same symbol).

Our objective was initially to probe the PSD of different polymer samples from T_2 measurements at room temperature, followed by applying eq 5 (assuming cylindrical pore geometry, i.e., $S/V = 2/R$, with R equal to the pore radius). However, this approach failed, in the sense that PSD determined from NMR relaxometry was significantly different from the PSD derived from N_2-adsorption measurements (not shown). Such a lack of resemblance in PSDs derived from these different experimental techniques originates from a complex interplay between molecular diffusion, the degree of pore connectivity, and potential distribution of paramagnetic impurities on the pore surface.[29]

If extending the "single-pore" relaxation model (eq 5) to a system of multiple (discrete number N) pores, the (normalized) transversal magnetization $M(t)$, may be written[29]

$$M(t) = M_0 \sum_{i=1}^{N} P_i \exp\left[-\frac{1}{T_{2i}} \cdot t\right] \quad (6)$$

where P_i is equal to the volume fraction of water within pore i. For a continuous PSD, this sum can be converted into an integral

$$M(t) = M_0 \int_0^{\infty} P(T_2) \exp\left[-\frac{t}{T_2}\right] dT_2 \quad (7)$$

where $P(T_2) dT_2$ now represents the volume fraction of water having relaxation times within the interval T_2 to $(T_2 + dT_2)$. The corresponding distribution $P(T_2)$ can be obtained by an inverse Laplace transform of the time dependent magnetization $M(t)$, commonly performed numerically with the CONTIN program. In this work we have used a Window-based toolbox software denoted RIWinDXP, which is a Resonance Instrument Windows Distributed EXPonential analysis software dedicated to the Maran Ultra series. The resulting S/V ratio may be derived by applying eq 5.

At this point it is of importance to emphasize that the success of determining the S/V ratio relies on the complex interplay between instrumental setting (the interpulse timing 2τ between successive π-pulses in the CPMG pulse sequence), PSD, PC, and diffusivity (D) of the pore-confined molecules.

For instance, if applying a CPMG experiment on water confined in a porous material at room temperature, and denoting the diffusivity of water by D and the interpulse timing by 2τ, it follows from the Einstein equation that water molecules within a distance R ($=\sqrt{6D \cdot 2\tau}$) from the surface will have sensed the surface during time 2τ. Inserting $D_{\text{water}} = 2.3 \times 10^{-9}$ m^2/s[32] and $2\tau = 60 \times 10^{-6}$ s (the minimum accessible value of τ) gives $R \approx 9 \times 10^3$Å, which suggests that a water molecule within the polymer sample will have experienced the pore wall many times during the time of the experiment. If cooling the polymer sample to 258 K, the diffusivity will decrease to approximately 0.6×10^{-9} m^2/s,[32] resulting in a root-mean-square displacement R of approximately 5000 Å, which is still much larger that the pore dimension.

Consider a connected pore system composed of two pores of radii R_1 and R_2 (R_1, $R_2 \ll 10^4$ Å), surface areas S_1 and S_2, and volumes V_1 and V_2, between which water molecules diffuse freely (high degree of pore connectivity).

It follows that the S/V ratio of such a system can be written $S/V = [S_1 + S_2]/[V_1 + V_2]$, which for spherical pores with $R_2 = \alpha R_1$ ($\alpha > 1$) and $R_1 = 3$ (without loss of generality) simplifies to $S_1/V_1 = 1$, $S_2/V_2 = 1/\alpha$. In particular, for water-saturated pores possessing high PC and fast diffusivity, the S/V ratio derived from NMR relaxometry will be $S/V = (1 + \alpha^2)/(1 + \alpha^3)$, which might be significantly biased with respect to the true S/V ratio of the smaller pores. The last equation shows that this biasing will become more pronounced with increasing α, i.e., when the difference in pore dimension between the two pores increases.

To determine T_2 we must decide which relaxation model to activate, i.e., the discrete relaxation model (eq 6) or the continuous relaxation model (eq 7). After some trial and error we found the discrete relaxation model, with four exponential terms ($N = 4$ in eq 6), to result in a random error distribution between model-fitted and observed relaxation times. However, the resulting temperature−relaxation rate behavior was difficult, if not impossible, to rationalize.

We next reduced the number of exponential terms by one, for which a 3-exponential model-fit ($N = 3$) is shown in Figure 5 at two different temperatures, 234 and 272 K, respectively.
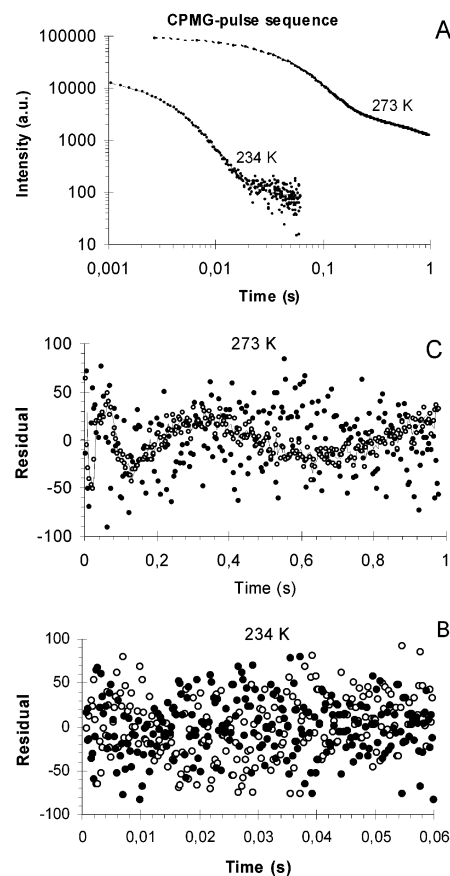

Figure 5. (A) Signal intensity versus time, as obtained from a CPMG pulse sequence ($2\tau = 60$ μs) at two different temperatures, 234 and 272 K. The dotted curves represent model fits to a discrete model, composed of a sum of three exponential functions, and a continuous model representation, respectively. The residuals between observed and model fitted (the discrete relaxation model ($\bigcirc$; eq 6) and the continuous relaxation model ($\bullet$; eq 7)) signal intensities are plotted in panels B and C, at two different temperatures, 234 and 272 K, respectively.

On the same figure a continuous model-fit (eq 7) is shown, as well. As can be inferred from the residual plot (Figure 5C), the discrete model-fit reveals a *slight* but significant nonrandom error distribution with increasing temperature. On this ground, we decided to use the continuous relaxation model throughout in this work (because this model demonstrates random error distributions).

A selection of relaxation time distributions (dI/dT_2) of water confined in sample S107 as a function of temperature is plotted in Figure 6.

Of particular interest is the relaxation time distribution derived for short T_2 times (regions a′ and a in Figure 6) of which an expanded view is shown in Figure 7 at $T = 248$ K.

Within experimental error, the smaller peak (region a′) shows no variation in either intensity or relaxation rate when increasing the temperature from 238 K (the lowest attainable temperature) up to a temperature at which additional solid ice starts melting ($\sim$260 K). When increasing the temperature further, the signal intensity (region a′) decreases, while the relaxation time remains approximately constant. When all solid ice has melted, this peak is no longer detectable. On this ground we tentatively assign this relaxation band (region a′) to interface water, which exists within any pore before onset of melting of solid ice. As already pointed out, the average signal intensity of this peak was estimated to be approximately (1.6 ± 0.4)%, relative to the signal intensity of all pore water within the sample, as measured
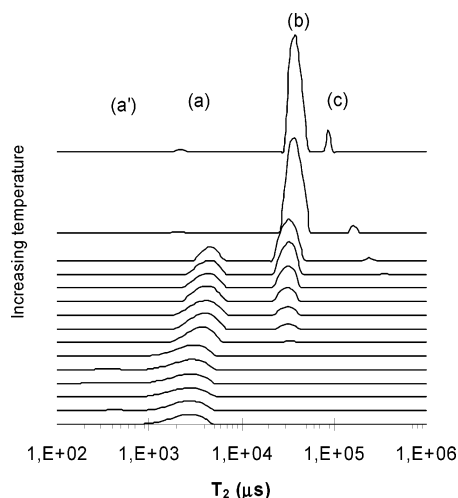
Pore Morphology of Porous Polymer Particles

J. Phys. Chem. B, Vol. 109, No. 51, 2005 **24299**

Figure 6. Relaxation time distribution (dI/dT_2) versus temperature of pore confined water in sample S107. The figure displays only a limited number of distributions, for clarity. Temperature is increasing from bottom to top (238, 242, 247, 252, 257, 265, 266, ..., 271, 272, 274 K).
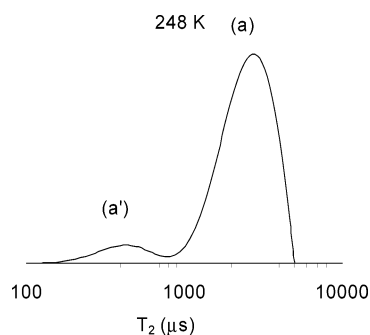

Figure 7. A typical example of the relaxation time distribution, dI/dT_2, of pore confined water (sample 107) at "low" temperature (see Figure 5).
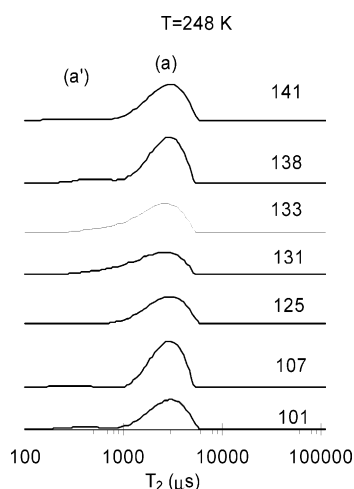

Figure 8. T_2-distribution of water confined in the smaller pores within different polymer samples (similar to sample S107) at $T = 248$ K.

just above the melting point of bulk water. The corresponding relaxation time is symbolized by T_{2S} and is assigned to the relaxation time of surface water, i.e., $T_{2S} = (394 \pm 36)$ μs.

The relaxation time distribution of six additional, but different polymer samples was determined at the lower temperature (248 K) and the results are depicted in Figure 8. The average relaxation time of water within the smaller pores, region a (Figure 7), was calculated from eq 8 and plotted against the
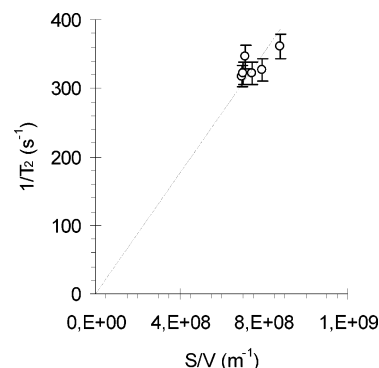

Figure 9. The spin–spin relaxation rate ($1/T_2$) of water as a function of the S/V ratio confined in the smaller pores (region a), as obtained from six different polymer samples. The straight line was fitted by constraining the fit, i.e., (S/V, $1/T_2$) = (0, 0.4 s^{-1}), according to eq 5.

S/V ratio (Figure 9), as obtained from N_2-adsorption measurements (Table 2).

Surface Relaxation Strength (ρ_2). The parameter ρ_2 in eq 5 is characteristic of the fluid–surface interaction strength and depends on the surface chemistry of the material. Hence, it is expected to vary significantly between different porous systems, even for the same pore confined fluid (water in this work). The surface relaxation strength ρ_2 may be determined from the slope of a straight line, represented by eq 5A (see Figure 9). Since the S/V ratio of bulk water is equal to 0, the straight line must go through the point (S/V, $1/T_2$) = (0, 0.4), resulting in $\rho_2 = (0.44 \pm 0.01) \times 10^{-6}$ ms^{-1}. This value is somewhat larger than that presented recently by Valckenborg et al. ($\rho_2 = (0.11 \pm 0.01) \times 10^{-6}$ ms^{-1}) on water confined in silica gels[17] but smaller than that reported by Kleinberg et al. ($\rho_2 = (2-4) \times 10^{-6}$ ms^{-1})[33] on water confined in synthetic calcium silicates.

Of particular importance, Bryar et al.[34] reported that ρ_2 may vary within the range of 10^{-9} to 10^{-4} ms^{-1}. In particular, the existence of paramagnetic sites on a surface may significantly enhance the surface relaxivity, suggesting that NMR relaxation measurements are so sensitive to paramagnetic impurities that most natural samples will probably have ρ_2 values above 1×10^{-6} m/s.[34] Hence, our polymer sample seems to be relatively free of such paramagnetic impurities. Moreover, since the relaxation time is dependent on temperature, the surface relaxivity will be dependent on temperature, as well.

It is worth mentioning that the susceptibility difference between a porous matrix and a pore-confined fluid generates internal gradients, which become increasingly more significant with increasing magnetic field strength and thus makes T_2 measurements more difficult and time-consuming to carry out. Actually, it was reasonably worthless to estimate T_2 prior to the introduction of low-field NMR techniques.

Thickness (λ) of the Interface Layer and PSD. Applying eq 5A, the thickness λ of the surface layer was calculated to give $\lambda = (1.73 \pm 0.20)$ Å, corresponding to approximately one molecular layer of water. Such a thickness is of the same order as reported by other researchers in the field.[22,35]

The PSD for the smaller pores, as derived from relaxation time measurements and N_2-adsoption measurements, are shown in Figure 10, and are in reasonable agreement, when considering that the former distribution was derived for a dry sample while the latter distribution was derived for a water-saturated sample.

It has to be emphasized that the results shown in Figure 10 are based on the assumption that the pores are cylindrical in shape and that the S/V ratio of the smaller pores is the same for
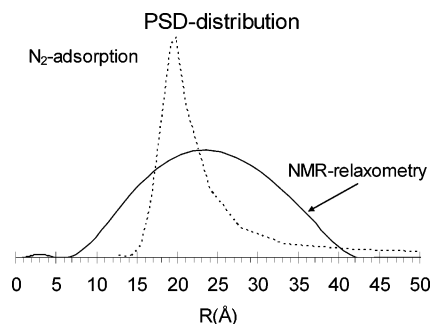
Figure 10. PSD for the smaller pores (region A), as derived from relaxation time (—) and N_2-adsorption measurements (···), at low temperature. See text for further details.

a dry sample and the same sample saturated with water, respectively.

Gibb−Thompson Equation and the Parameter K. We now address the question of how to determine the parameter K in eq 2 from relaxation time measurements. Unfortunately, the available NMR instrument was not capable of generating temperatures less than approximately 238 K, implying that it was not possible to determine the actual melting transition temperature of ice within the smaller pores (region A in Figure 4) by NMR cryoporometry. If possible, however, this parameter (K) could be simply estimated from eq 2 by inserting the pore size R (=25.3Å), as determined from N_2-adsorption. However, the parameter K may be determined by using a different approach, i.e., by combining NMR relaxometry and N_2-adsorption measurements.

As inferred from the T_2-distribution curves (Figure 6), they may be classified according to their number of distinct and separate distribution components. At low temperature, they reveal basically a single, narrow distribution (phase a) component, two separate but distinct components at intermediate temperatures (phases a and b), and a single component (phase b) at higher temperatures. The average relaxation rates ($1/T_{2X}$ with X = a and b) and corresponding intensities (I_X with X = a and b) as functions of temperature can be calculated from eq 8

$$T_{2,av} = \int_{T_{2,lower}}^{T_{2,upper}} T_2 \cdot [\mathrm{d}I/\mathrm{d}T_2] \, \mathrm{d}T_2 / \int_{T_{2,lower}}^{T_{2,upper}} [\mathrm{d}I/\mathrm{d}T_2] \, \mathrm{d}T_2 \quad (8A)$$

$$I = \int_{T_{2,lower}}^{T_{2,upper}} [\mathrm{d}I/\mathrm{d}T_2] \, \mathrm{d}T_2 \quad (8B)$$

The results are shown in Figure 11. As can be inferred from this figure, only a single component (phase a) appears at temperatures lower than approximately $T = T_C = 267$ K ($X_C = 1000/T = 3.77$ K^{-1}). A more detailed examination of this phase is possible by referring to Figure 12.

For example, for temperature $T < T_C$ the width of the T_2-distribution within "phase-a" remains constant and independent of temperature, suggesting that water within the smaller pores (A-pores) exchanges rapidly with water formed in region B upon heating.

That water within B-pores actually exchanges with water in A-pores is supported by the observed reduction in relaxation rate ($1/T_{2a}$) and the increase in intensity (I_a) of the phase a water with increasing temperature. This suggests that within the actual temperature range, the S/V ratio can be uniquely defined via eq 9, in which I_X (X = A and B) denotes the intensity of water within A-pores and B-pores, respectively, and R_X (X = A and B) represents the cylindrical pore radius
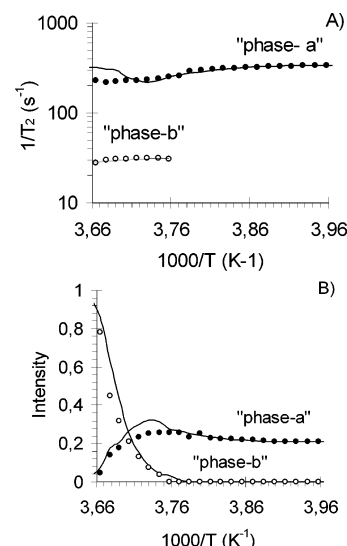

Figure 11. Average relaxation rates and corresponding intensities of phases a and b, as determined from the relaxation distributions in Figure 6, via eq 9. The solid curves represent model calculations, and will be discussed in a later section.

within region X (see Table 3);

$$\frac{S}{V} = \frac{S_A + S_B}{V_A + V_B} = \frac{2\pi R_A \cdot I_A + 2\pi R_B \cdot I_B}{\pi R_A^2 \cdot I_A + \pi R_B^2 \cdot I_B} =$$

$$2\frac{R_A \cdot I_A + R_B \cdot I_B}{R_A^2 \cdot I_A + R_B^2 \cdot I_B} = \frac{T_{2S}}{T_2} \cdot \frac{1}{\lambda} \quad (9)$$

The expression on the right-hand side of eq 9 is derived from eq 5. Inserting $I_A = 0.22$ (Figure 12), $R_A = 25.3$ Å (Table 2B), $R_B = K/\Delta T_B$ (eq 2, with $\Delta T_B = 6.77$ K; Table 3), and I_B (=$I_b - I_A$) as derived from Figure 12, the parameter K can be calculated at any temperature within the defined temperature region ($T < T_C$). From the data presented in Figure 12, seven K values were derived (eq 9) within the temperature range 268 K > T > 259 K, at which temperature component B contributes with 3−20% of the total water content. The resulting average value of K was calculated to be $K = (420 \pm 50)$ KÅ and is consistent with corresponding values reported in the literature, which are ranging from 410 to 730 KÅ.[15−17] To the best of our knowledge, this approach represents the first attempt to estimate K from a combined use of cryogenic NMR and NMR relaxometry.

Theoretically, K depends only on the physical properties of the pore-confined fluid. The agreement between the K-value obtained in the present analysis and the corresponding value reported in the literature[15−17] supports the analytical approach applied and discussed above.

A minor observation concerns the slight, however significant decay of the relaxation curve with increasing temperature at low temperatures (Figure 12B). This is a pure temperature effect, since the signal intensity remains constant, and originates from a thermally activated molecular process, related to the molecular motion of water within the pores. The activation energy was found to be $\Delta E = (43 \pm 4)$ J/mol and was implemented in the above analysis. However, the discussion of molecular dynamics will be the subject for further studies and will not be discussed any further in this work.

Note, the melting point distribution curve $\mathrm{d}I_A/\mathrm{d}X$ of water confined in the A-pores can be determined from the relaxation rate distribution curve $\mathrm{d}I/\mathrm{d}T_{2A}$ (Figure 7), which is obtained by

Pore Morphology of Porous Polymer Particles

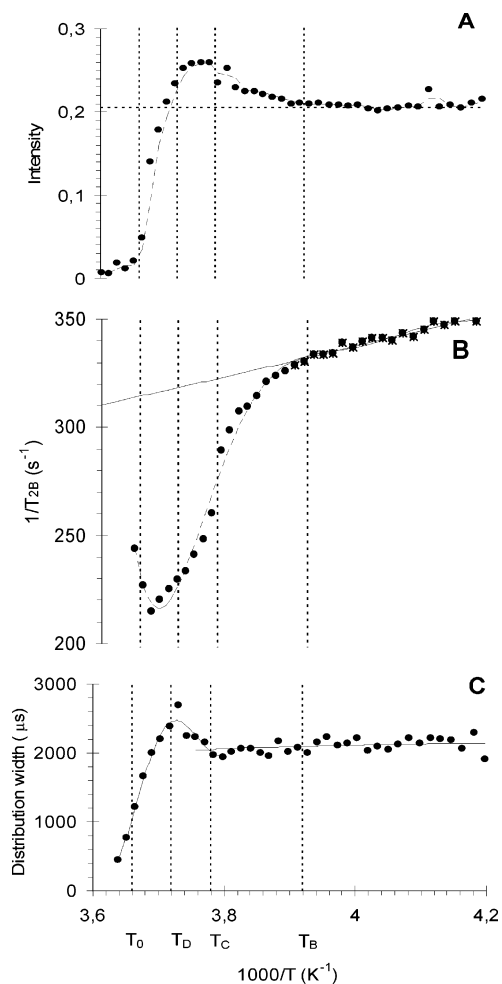*J. Phys. Chem. B, Vol. 109, No. 51, 2005* **24301**

Figure 12. Temperature behavior of (A) the signal intensity, (B) the relaxation rate $1/T_2$, and (C) the width of the relaxation time distribution of water confined in "phase a". See text for further details.

a simple algebraic manipulation, eq 10:

$$\frac{dI_A}{dX} = \frac{dI}{dT_{2A}} \cdot \frac{dT_{2A}}{dR} \cdot \frac{dR}{dX} \qquad (10)$$

where the terms dR/dX and dT_2/dR can be explicitly derived from eqs 2 and 5.

Pore Morphology. From NMR cryoporometry four different and distinct regions A, B, C, and D (Figure 4) are identified. Each region reflects a temperature region in which pore-confined solid water (ice) melts, which in turn relates to four distinct pore size regions (pore-A, pore-B, pore-C, and pore-D) by applying eq 2. If these pore regions were completely isolated, i.e., the pores were nonconnected, no exchange of water would take place between the pore regions, resulting in four different and distinct relaxation rates, one relaxation rate for each pore region.

As already pointed out, at any temperature the overall relaxation time distribution is essentially resolved in one or two distinct subdistributions, demonstrating that exchange of water (on the NMR time scale) takes place between some or all pore regions A, B, C, and D (Figure 6). In particular, these results indicate that unique and distinct pore sizes cannot be extracted from NMR relaxometry alone, and represent a frequently occurring problem when aimed at deriving PSD from NMR relaxometry of pore confined fluids.

However, combining NMR cryoporometry and NMR relaxometry, information regarding both PC and PSD may be derived.

To gain this information, we must explore how water within the four different space regions (derived from cryogenic NMR) distributes between the two phases "a" and "b" (derived from NMR relaxometry) during heating of the sample. In so doing, we will assume that water within each of the two phases "a" and "b" exchanges fast on the NMR time scale, thus resulting in two distinct relaxation rates $1/T_{2a}$ and $1/T_{2b}$ with corresponding intensities I_a and I_b. The resulting equations are summarized below:

$$1/T_{2a} = I_A f_A \cdot 1/T_{2A} + I_B f_B \cdot 1/T_{2B} + I_C f_C \cdot 1/T_{2C} + I_D f_D \cdot 1/T_{2D} \qquad (11A)$$

$$1/T_{2b} = I_A(1 - f_A) \cdot 1/T_{2A} + I_B(1 - f_B) \cdot 1/T_{2B} + \\ I_C(1 - f_C) \cdot 1/T_{2C} + I_D(1 - f_D) \cdot 1/T_{2D} \qquad (11B)$$

$$I_a = f_A \cdot I_A + f_B \cdot I_B + f_C \cdot I_C + f_D \cdot I_D \qquad (11C)$$

$$I_b = (1 - f_A) \cdot I_A + (1 - f_B) \cdot I_B + (1 - f_C) \cdot I_C + (1 - f_D) \cdot I_D \qquad (11D)$$

The parameter f_X (X = A, B, C, and D) reflects the fraction of water (in pore X) that distributes between phases "a" and "b". In addition, the following normalization constraint is used:

$$I_A + I_B + I_C + I_D = 1 \qquad \text{at } T = 273.15 \text{ K} \qquad (11E)$$

which results in an over-determined set of five equations in four unknowns f_X (X = A, B, C and D) at all temperatures. The model fitted results are represented as solid curves in Figures 11. The experimental data are shown as black and open circles, respectively.

The above approach certainly represents an approximation, since T_2 of water within each of the two phases "a" and "b" is not single-valued, but characterized by narrow distributions (see Figure 6). Only their mean values, as calculated by a weighted averaging procedure over the respective distributions (eq 8), are plotted in Figure 11. Also, the relaxation rates $1/T_{2X}$ (X = A, B, C, and D; eq 11) represent average relaxation rates and were calculated from eq 5 (assuming cylinder pore geometry) and eq 2 (in combination with the data presented in Table 3).

Figure 11 reveals some significant difference between observed and model-fitted relaxation rates at certain temperatures. This discrepancy is believed to emanate from certain model assumptions, which must be considered as approximations: (1) average relaxation rates ($1/T_{2X}$; X = A−D) rather than distributions have been used in the model calculations, (2) fast exchange of water within both phases "a and b" is assumed, and (3) no exchange of water between phases "a and b" takes place.

For instance, at a temperature of $T \approx 267$ K (X = $1000/T$ = 3.74 K^{-1}) component C appears within phase "a". However, upon further warming to $T \approx 269$ K (X = $1000/T$ = 3.71 K^{-1}) this phase disappears without reappearing in phase "b". Hence, we believe that the appearance of component C in the former phase is a numerical artifact originating from the inherent simplifications and assumptions made in the model calculations and conclude that only components A and B appear in phase "a". Within these approximations, the derived pore structure (Figure 14) must be considered with some care and will be discussed next.

Considering Figure 13B, only water in regions A and B contributes to phase "a". Upon warming to $T \approx 272$ K (X = $1000/T$ = 3.68 K^{-1}) these components disappear completely from phase "a", and reappear in phase "b". The reason for this
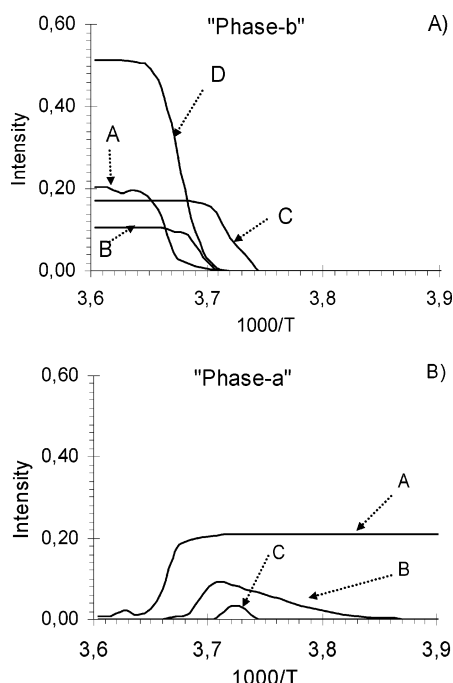
Figure 13. Illustration of how water within the four distinct pore regions A, B, C, and D (as observed from NMR cryoporometry; Figure 4) distributes between the two phases "a and b" (as observed from NMR relaxometry; Figure 6) as a function of temperature. See text for further details.

Figure 14. Illustration of a "quarter" of the pore structure within the polymer particles investigated in this work, as probed by a combined use of NMR cryoporometry and NMR relaxometry. The pore D ($R_D = 560$ Å) is surrounded by pores A ($R_A = 25$ Å), B ($R_B = 62$ Å), and C ($R_C = 82$ Å), where R_X (X = A, B, C, and D) represents a cylindrical pore radius.

is that water from the former phase exchanges with water from the D-pores. Since at high temperature only a single T_2 distribution is observed ("phase b") all pores are actually connected. However, the results presented in Figure 13 suggest that there is no direct connectivity between AB-pores and C-pores, because this would result in the appearance of a C-peak within "phase-a", which is not observed. Actually, the connectivity between AB and C is mediated by pores D.

From the intensity distributions in Figure 13A,B, the percentage of B-pores taking part in this network (A-B-D-pores) is calculated and amounts to approximately 82%. In contrast, the contribution from the A-pores is only marginal, and approximately 10%.

In general, the relative number of X and Y pores (N_X/N_Y) within a network can be calculated from the observed signal intensities I_X and I_B, according to eq 12, if assuming cylinder geometry:

$$\frac{N_X}{N_Y} = \frac{I_X}{I_Y} \cdot \frac{\pi R_Y^2}{\pi R_X^2} \tag{12}$$

Inserting numerical values for R_A (=25 Å; Table 3), R_B (=62 Å; Table 3), and I_X (X = A and B; Figure 13A, B), N_A/N_B becomes equal to 1.1 ≈ 1. In short, the relative number of A- and B-pores within the connected network A-B-D is approximately 1:1.

When referring to Figure 13A, water in pore C appears in phase "b" at a temperature T of approximately 267 K ($X = 3.74$ K^{-1}). As recently noticed, no water from pore C is observable in phase "a", implying that there is no "direct" connectivity between A- and C-pores or between B- and C-pores. If a direct coupling between C-pores and A-pores exists, an increase in the signal intensity of water within A-pores is expected to be seen along with the signal intensity of water within the C-pores appearing in "phase b". However, no such
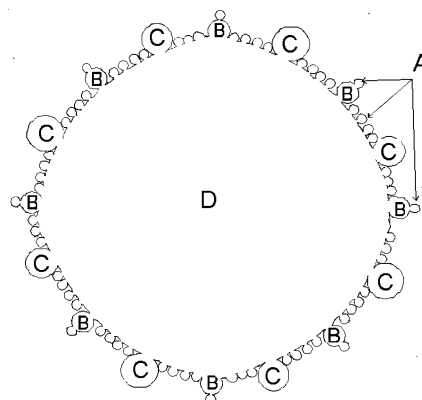
signal of water within the A-pores is observed. Again, the connectivity between pore A and pore C is mediated via pore D. Upon further warming ($T \approx 272$ K ($X = 1000/T = 3.68$ K^{-1})) of the sample a significant increase in the intensity of water within the D-pores appears, implying that C- and D-pores are connected (due to the implicit assumption of fast exchange of water within both phases "a" and "b"). The relative number of C-pores contributing to the C−D connectivity is estimated from the intensities in Figure 13B and amounts to approximately 82%.

Likewise, the relative number of B- and C-pores connected to a D-pore can be estimated from Figure 13A,B in combination with eq 12 ($R_C = 82$ Å) and results in $N_C/N_B = 1.0$.

Moreover, as can be inferred from the data in Figure 13A, a significant increase in the intensity of water from both A-pores and D-pores appears close to the bulk melting point of pure solid ice, implying that also A- and D-pores are connected. Nearly 90% of the A-pores contribute to this C-D connectivity. According to eq 12, the relative number of A- and B-pores connected to D-pores can be estimated, and results in $N_A/N_B = 12.7 \approx 13$.

Taking the average pore radius of a D-pore to be equal to 560 Å (Table 3), we obtain the average pore structure shown in Figure 14, which explains more than 80% of the observed intensity distribution in Figure 13.

Unfortunately, the actual pore size of region D, as derived from NMR cryoporometry ($R_D = 560$ Å; Table 3), is rather uncertain due to two effects: (1) the melting point of solid ice within the D-pore (272.4 K) is too close to the melting point of bulk ice and (2) the uncertainty in the estimated melting point of pore confined ice is too large (±0.5 K).

Moreover, NMR relaxometry is of little help to resolve this enigma due to exchange of water between pores, as discussed thoroughly in this paper.

However, whatever the actual pore size of a D-pore, the relative distribution of AB-, C-, and A-pores connected to a D-pore will be in the approximate ratio 1:1:13; the overall pore structure may be designed, see Figure 14.

Conclusions

NMR cryoporometry in combination with N$_2$-adsorption (reference technique) enables the PSD within porous materials to be established. The difference in PSD obtained by NMR cryoporometry and NMR relaxometry, respectively, is symp-

Pore Morphology of Porous Polymer Particles

J. Phys. Chem. B, Vol. 109, No. 51, 2005 **24303**

tomatic for an exchange of water (diffusion controlled) between different pore regions (on an NMR time scale). The results presented in this work suggest that a combined use of these two rather different NMR techniques may probe the actual PC. In general, if cryogenic NMR cryoporometry displays N different pore regions and the NMR relaxometry reveals M different and distinct relaxation times, or "phases" ($M \leq N$), a fraction f_X (or distribution number) of water within the different pore regions X (=1, 2, ..., N) will distribute between the M different phases. These distribution numbers can be solved uniquely if the number of equations is larger than or equal to the number of distribution numbers, i.e., $2M + 1 \geq N$. The last equation (equation $2M + 1$) defines the normalization condition (see eq 11E). For the polymer system investigated in this work N was equal to 4 and M equal to 2.

By analyzing the resulting intensity distributions (N) of water between the different phases (M), it should in theory be possible to construct a geometric pore model.

As a spin-off, the surface relaxivity (ρ_2), the parameter K (eq 2), and the thickness λ of the inter-phase fluid layer, located between the solid matrix and the solid fluid within the pore, may be extracted.

References and Notes

(1) MacElroy, J. M. D. *Korean J. Chem. Eng.* **2000**, *17* (2), 129.

(2) Turro, N. J.; Lei, X.-G.; Wei, L.; Zhiqiang, L.; McDermott, A.; Ottaviani, M. F.; Abrams, L. *J. Am. Chem. Soc.* **2000**, 1*22* (47), 11649.

(3) MacElroy, J. M. D.; Pozhar, L. A.; Suh, S.-H**.** *Colloids Surf., A* **2001**, *187−188*, 493.

(4) Poulet, G.; Sautet, P.; Tuel, A. *J. Phys. Chem. B* **2002**, *106* (34), 8599.

(5) Hagslatt, H.; Jonsson, B.; Nyden, M.; Soderman, O. *J. Magn. Reson.* **2003**, *161* (2), 138.

(6) Frunza, L.; Kosslick, H.; Pitsch, I.; Frunza, S.; Schoenhals, A. *J. Phys. Chem. B* **2005**, *109* (18), 9154.

(7) Sahimi, M.; Tsotsis, Theodore T. J. *Catalysis* **1985**, *96* (2), 552.

(8) Qiao, Y.; Schoenhoff, M.; Findenegg, G. H. *Langmuir* **2003**, *19* (15), 6160.

(9) Sahasrabudhe, A.; Mitra, S.; Tripathi, A. K.; Mukhopadhyay, R.; Gupta, N. M. *Phys. Chem. Chem.* Phys. **2003**, *5* (14), 3066.

(10) Ishimaru, S.; Ikeda, R. *Recent Res. Dev. Mol. Struct.* **2002**, *1*, 143.

(11) Topgaard, D.; Søderman, O. *J. Biophys.* **2002**, *83*, 3596.

(12) Mitchell, J.; Stark, S. C.; Strange, J. H. *J. Phys. D*: *Appl. Phys.* **2005**, *38* (12), 1950.

(13) Ren, X.; Stapf, S.; Kuhn, H.; Demco, D. E.; Blumich, B. *Magn. Reson. Imaging* **2003**, *21* (3/4), 261.

(14) Allen, S. G.; Stephenson, P. C. L.; Strange, J. H. *J. Chem. Phys*. **1998**, *108* (19), 8195.

(15) Strange, J. H.; Mitchell, J.; Webber, J. B. W. *Magn. Reson. Imaging* **2003**, *21*, 221.

(16) Valckenborg, R.; Pel, L.; Kopinga, K. *Magn. Reson. Imaging* **2001**, *19* (3−4), 489.

(17) Valckenborg, R. M. E.; Pel, L.; Kopinga, K. *J. Phys. D*: *Appl. Phys.* **2002**, *35* (3), 249.

(18) Webber, J. B. W.; Strange, J. H.; Dove, J. C. *Magn. Reson. Imaging* **2001**, *19*, 395.

(19) Jackson, C.; McKenna, G. *J. Chem. Phys*. **1990**, *93*, 9002.

(20) Ishimaru, S.; Ikeda, R. *Recent Res. Dev. Mol. Struct.* **2002**, *1*, 143.

(21) Strange, J. H.; Rahman, M.; Smith, E. G. *Phys. Rev. Lett.* **1993**, *71* (21), 3589.

(22) Schmidt, R.; Hansen, E. W.; Stoecker, M.; Akporiaye, D.; Ellestad, O. H. *J. Am. Chem. Soc.* **1995**, *117* (14), 4049.

(23) Overloop, K.; Van Gerven, L. *J. Magn. Reson., Ser. A* **1993**, *101* (2), 179.

(24) Brownstein, K.; Tarr, C. *Phys. Rev.* **1979**, *71*, 3589.

(25) D'Orazio, F.; Tarcson, J. C.; Halperin, W. P.; Eguchi, K.; Mizusaki, T. *J. Appl. Phys.* **1989**, *65*, 742.

(26) Shull, G. C. *J. Am. Chem. Soc.* **1948**, *70*, 1404.

(27) Gibbs, J. W. *The Collected Works of J. Williard Gibbs;* Academic Press: New York, 1928. Thompson, W. (Lord Kelvin) *Philos. Mag.* **1871**, *42*, 448.

(28) Gallegos, D. P.; Munn, K.; Smith, D. M.; Stermer, D. L. *J. Colloid Interface Sci.* **1986**, *119*, 127.

(29) Cohen, M. H.; Mendelsohn, K. S. *J. Appl. Phys.* **1982**, *53*, 1127.

(30) Brown, R. J. S.; Borgia, G. C.; Fantazzini, P.; Mesini, E. *Magn. Reson. Imaging* **1991**, *9*, 687.

(31) Kleinberg, R. L.; Kenyon, W. E.; Mitra, P. P. *J. Chem. Phys.* **1998**, *108*, 9195.

(32) Price, W. S.; Ide H.; Arata, Y. *J. Phys. Chem. A* **1999**, 448.

(33) Foley, I.; Farooqio, S. A.; Kleinberg, R. L. *J. Magn. Reson., Ser. A* **1996**, *123*, 95.

(34) Bryar, T. R.; Daughney, C. J.; Knight, R. J. *J. Magn. Reson.* **2000**, *142*, 74.

(35) Hollemann, A.; Wiberg, E.; Wiberg, N. *Lehrbuch der Anorgaischen Chemie*; DegruyterB: Berlin, Germany, 1995; Vol. 101.